scientific reports

Check for updates

OPEN

First experimental verification of prompt gamma imaging with carbon ion irradiation

Aicha Bourkadi Idrissi[1,2]✉, Giacomo Borghi[1,2], Anita Caracciolo[1,2], Christian Riboldi[1,2], Marco Carminati[1,2], Marco Donetti[3], Marco Pullia[3], Simone Savazzi[3], Franco Camera[2,4] & Carlo Fiorini[1,2]✉

Prompt Gamma Imaging (PGI) is a promising technique for range verification in Particle Therapy. This technique was already tested in clinical environment with a knife-edge-collimator camera for proton treatments but remains relatively unexplored for Carbon Ion Radiation Therapy (CIRT). Previous FLUKA simulations suggested that PG profile shifts could be detected in CIRT with a precision of $\sim$ 4 mm (2σ) for a particle statistic equal to $5 \cdot 10^7$ C-ions using a 10 × 10 cm^2 camera. An experimental campaign was carried out at CNAO (Pavia, Italy) to verify these results, using a knife-edge-collimator camera prototype based on a 5 × 5 cm^2 pixelated LYSO crystal. PG profiles were measured irradiating a plastic phantom with a C-ion pencil beam at clinical energies and intensities, also moving the detector to extend the FOV to 13 × 5 cm^2. The prototype detected Bragg-peak shifts with $\sim$ 4 mm precision for a statistic of $\sim 4 \cdot 10^8$ C-ions ($3 \cdot 10^8$ for the extended FOV), slightly larger than expected. Nevertheless, the detector demonstrated significant potential for verifying the precision in dose delivery following a treatment fraction, which remains fundamental in the clinical environment. For the first time to our knowledge, range verification based on PGI was applied to a C-ion beam at clinical energy and intensities.

Particle Therapy (PT) is a developing field of radiation therapy (RT) in which protons, heavy ions (e.g. carbon ions) or neutrons are used to selectively irradiate tumors reducing tissues toxicity with respect to standard radiotherapy. With more than one hundred clinical particle therapy facilities operating worldwide in 2023[1], this technique has known a rapid progress and widespread use in recent years[2].

X-rays and electron beams, commonly used in radiation therapy, deposit a dose that decreases with depth, following an exponential law in the case of x-rays. Heavy charged particles passing through a material, instead, gradually lose their kinetic energy (and deposit the dose) via Coulomb interactions with atomic electrons. Since linear energy transfer (LET) or stopping power is approximately proportional to the inverse of the square of their velocity, depth-dose profiles of charged-particle beams rise sharply near the end of their range and then have a steep distal fall-off, which is known as a Bragg peak. In charged-particle beam therapy, the Bragg peak position is adjusted to the depth of the tumor to reduce radiation exposure to surrounding normal tissues and side effects from the treatment.

However, despite the potential advantages in terms of accuracy and tumor coverage, PT is not without challenges since various sources of uncertainty may determine a mismatch between the planned position of the peak of the deposited dose and its actual position. These uncertainties include anatomical variation of the patient (e.g. tumor shrinkage, weight loss, changes in tissue density due to swelling or filling of cavities), physiological movements of organs (e.g. breathing or bladder filling), and patient mispositioning, which are also present in traditional radiotherapy with photons but to which PT is more sensitive due to its more peaked dose profile. Other relevant sources of uncertainties are instead related to the calculation of the particle range in patients, e.g. due to the heuristic conversion from Computed Tomography (CT) number to particle Stopping Power Ratios (SPR)[3].

All these range uncertainties must be considered during treatment planning in PT, since errors in the calculation of the depth of the Bragg peak can dramatically affect the dose delivered to the tumor and to the healthy tissues nearby. To account for these uncertainties, safety margins are currently added to the tumor

[1]Dipartimento di Elettronica, Informazione e Bioingegneria (DEIB), Politecnico di Milano, 20133 Milan, Italy. [2]Istituto Nazionale di Fisica Nucleare, Sezione di Milano, 20133 Milan, Italy. [3]Centro Nazionale di Adroterapia Oncologica (CNAO), 27100 Pavia, Italy. [4]Dipartimento di Fisica, Università degli Studi di Milano, 20133 Milan, Italy. ✉email: aicha.bourkadi@polimi.it; carlo.fiorini@polimi.it

volume during treatment planning. In the case of deep-seated tumors, these margins might be considerable, up to 1 cm, which can limit the treatment selectivity[4–6]. For the same reasons, single irradiation fields presenting an organ at risk in the tumor distal region are usually avoided in favor of multiple irradiation fields to distribute the radiation dose more effectively, with the consequence of increasing the volume of irradiated healthy tissues[7].

To reduce these range uncertainties in PT, particle range in patients should be measured during the treatment (in-vivo range verification) in order to detect and, potentially, react to mismatches between the calculated and the real dose profile and therefore to fully exploit the advantages and the enhanced precision of PT[7,8]. Over the past decade, a multitude of researches have been carried on to develop different monitoring systems[9–12]. These systems strategically leverage the firmly established correlation between the particle range and the physical properties of secondary particles produced through nuclear interactions between the beam particles and the patient tissues.

In the context of particle therapy, distinct strategies have emerged, which are mainly based on the detection of three different products of the nuclear reactions between the ion beam and the patient tissues: β+ emitters, prompt gamma rays emitted by excited nuclei and charged fragments originating from the projectile or target nuclei fragmentation[13].

Positron Emission Tomography (PET) was one of the earliest methods for treatment monitoring which was proposed and clinically tested, either during the treatment or in the post-treatment phase. This method is based on the detection of coincident annihilation photons (511 keV gamma rays) resulting from the β+ decay of unstable nuclei produced during therapeutic irradiation[14]. Some of the challenges to be overcome when applying this technique are related to the long decay times of the most abundant positron emitters ($\sim$ 2–20 min), which would require to extend the image acquisition after the end of the treatment to maximize the acquisition of the signal, and the biologic washout of the signal over time, which instead degrades the correspondence between the dose delivered to the patient and the reconstructed activity image for long image acquisitions[15–18]. Despite these challenges, the INSIDE project has recently demonstrated in a clinical trial that in-beam PET imaging can be effectively used to monitor proton therapy treatments, while delivering the treatment and without extending the treatment time[19,20]. However, in order to achieve a response faster than the irradiation time, a large-acceptance and high-efficiency scanner would be required, which is not compatible with all possible patient irradiation configurations, especially in presence of a gantry. Clinical trials have been conducted also with therapeutic carbon ion beams, after the promising results obtained with tissue-like phantoms[21]. However, so far, PET performance resulted lower due to reduced statistics and short acquisition times[20].

Information on the position of the deposited dose can also be extracted by tracking the charged fragments emerging from the patients and reconstructing the distribution of their origin along the beam path, which is correlated with the delivered dose. Several groups developed advanced systems to apply this technique, e.g. using trackers based on hybrid silicon pixel detectors[22] or on several planes of scintillating fibers[23]. These systems demonstrated that this is a promising technique to effectively monitor inter-fractional range shifts during CIRT treatments. A performance test in clinically realistic conditions with an anthropomorphic head phantom demonstrated that the system based on silicon pixel detectors is sensitive to shifts of the fragment origins along the beam axis of at least 1.5 mm. The system based on scintillating fibers, instead, demonstrated in a clinical trial the capability to detect inter-fractional changes in the delivered dose. However, challenges remain in the application of this technique, especially for deep-seated tumors in which the fragments suffer from larger multiple scattering before emerging and therefore can provide less precise information.

Treatment verification relying on Prompt-Gamma (PG) radiation has also emerged as a promising approach for real-time range assessment during dose delivery[9,10,24]. Prompt gammas are secondary de-excitation photons emitted almost instantaneously (sub-ns scale) by excited nuclei, which are the products of nuclear reactions between the ions in the ion beam and the elements in the patients tissues. However, due to the high energies of such PG emissions, which are in the MeV range, it took several years of detector development to arrive at first viable prototypes of PG detection-based setups.

In these systems, range information can be extracted from energy (Prompt Gamma Spectroscopy, PGS[25,26]), temporal (Prompt Gamma Timing, PGT[27]), or spatial distribution (Prompt Gamma Imaging, PGI[28,29]) of the prompt gamma rays. In PGI measurements, the gamma spatial distribution can be obtained through an electronic or mechanical collimation of the photons reaching the detector. In the former approach, a Compton camera can be used[26,30–33] which enables to image a 3D PG vertex distribution, while in the second case mechanical collimators are used to select the gamma ray direction and obtain a 1D or 2D image of the PG distribution. Most common collimator designs are the knife-edge slit[29,34–36], multi-parallel slit[37] or pinhole collimators[38] but different approaches using structured collimator have also been proposed, such as in the case of the integration of a near-field coded mask technique using a maximum-likelihood expectation maximization algorithm to reconstruct the PG image[39,40] and of a multi-knife-edge slit collimator[41].

In recent years, there was a substantial progress in the development of PGI systems, mostly for application in proton therapy[9,11], which led at the beginnings of the 2010s to the development of the first knife-edge PGI system which could be used with a clinical beam current, capable to detect in a phantom Bragg-peak shifts below 4 mm at 2σ, with $0.5 \cdot 10^8$ incident protons at 100 MeV[35]. Since then, over the past decade, that system and other PGI systems based on mechanical collimation were developed and used in clinical trials for proton range verification, reaching range verification accuracies down to 1 mm[29,42,43].

C-ions have some undoubted advantages over protons in hadrontherapy thanks to their physical interaction properties that determine an higher linear energy transfer and therefore an higher relative biological effectiveness, leading to a better therapeutic effect on hypoxic tumors, which have a high resistance to radiation. However, C-ions also introduce additional challenges to apply the PGI technique: a higher neutron yield per ion and a smaller number of incident projectiles needed to provide a given physical dose compared to protons affect strongly the signal to background ratio[9]. The aforementioned factors make the optimization of detection

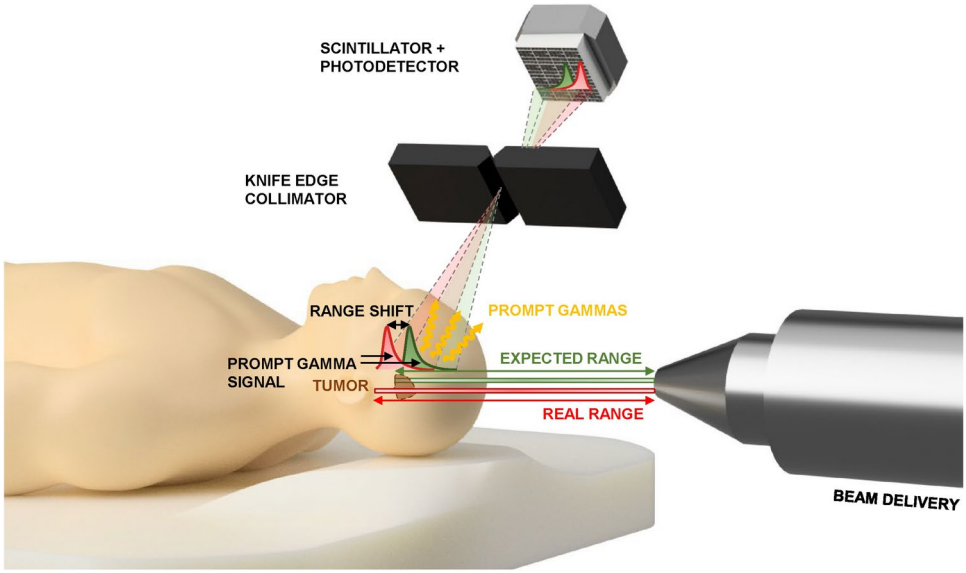

Fig. 1. Knife-edge slit camera concept of operation: deviations between real range and expected one are detected through PG signal projected to a pixellated camera thanks to a knife-edge slit collimator.

efficiency and gamma-neutron discrimination even more critical for the application of PGI to Carbon Ion Radiation Therapy (CIRT).

In this study, we thoroughly investigated the potential of PGI range verification in CIRT environment with a prototype of a knife edge slit-camera system to detect Bragg-peak shifts in a plastic phantom irradiated by a clinical C-ion pencil-beam.

In particular, the experimental work presented in this paper aimed at verifying the results of a previous Monte Carlo simulation campaign that was conducted through FLUKA, a general purpose Monte Carlo code for particle transport[44]. In those numerical simulations, a knife-edge slit camera was used to measure the secondary particles emitted in the 3–7 MeV energy range by a ICRP soft tissue phantom, emulating the patient irradiated with a mono-energetic pencil beam of C-ions of 150 MeV/u[45]. The energy was chosen to fit within the interval of therapeutic energies used in CIRT: indeed, at CNAO, a clinical carbon ion irradiation is characterized by an energy ranging from 120 to 400 MeV/u, while for protons the energy range is of 60–250 MeV[46]. The results suggested that range verification on a layer-by-layer approach could be possible using a 10 cm × 10 cm detection module, if the average number of primary particles delivered in a spill to cover a given layer of the tumor volume is about $5 \cdot 10^7$ ions.

In order to experimentally verify the results of the MC simulations, we developed and characterized an experimental setup to explore the PG fall-off retrieval capability with a pixelated knife-edge slit camera with a beam of C-ions at clinical energies. In this work, we conducted an experimental campaign at Centro Nazionale di Adronterapia Oncologica (CNAO) hadrontherapy center (Pavia, IT) where, to our knowledge, the first PGI measurement with carbon ions at clinical energy and intensities was carried out. Our work paves the way for implementing a PGI system for range verification in CIRT.

Methods

In a PGI system, the gamma camera detects the PG radiation emitted along the trajectory of the carbon-ion beam and provides a 1-D image of its distribution. The image is obtained projecting the radiation onto a position-sensitive detector through a knife-edge tungsten slit collimator. The goal is to identify any shifts in the PG profile, indicative of alterations in particle range, in order to ideally react to this variation to guarantee the safety of treatment delivery. Figure 1 illustrates the conceptual design of the system envisioned for operation in a clinical environment. In this work, a pixelated detector was chosen instead of the slab-based one used in simulations in order to develop a general-purpose PGI module, suitable not only for CIRT but also for proton therapy. In this application, higher segmentation of the detector is required in order to withstand higher count rates, since in some proton facilities the beam delivery is characterized by a much higher particle rate than for CIRT, which translates on a much higher rate of prompt gammas on the detector.

PGI camera system: design and calibration

The proposed camera comprises a tungsten-alloy knife-edge collimator and a scintillator detector based on a $Lu_{1.8}Y_{0.2}SiO_5$ (LYSO) pixelated crystal (SCIONIX (https://scionix.nl), Utrecht, Netherlands), which detects the projected distribution of prompt gammas. These materials are chosen for their favourable characteristics for PGI applications: the tungsten alloy (90% W–6% Ni–4% Cu) has high density and excellent machinability, while LYSO is a dense, fast scintillator with high light yield.

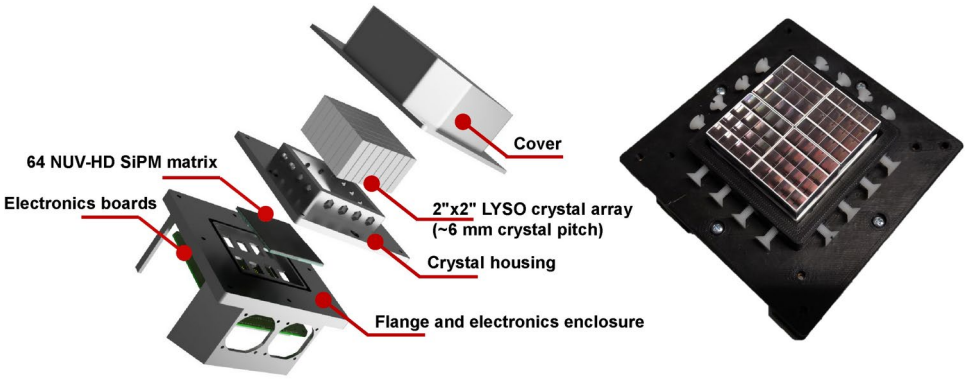

Fig. 2. 64-channel detector prototype for the experimental validation of PGI technique in CIRT.

The collimator (Fig. 3) is made of two separate blocks, has a thickness of 4 cm, a height of 12 cm and a width of 16 cm along the beam axis for each block. It features a knife-edge slit with adjustable width, which in this work has been set to 6 mm, and has a 63° aperture angle. The gamma detector, depicted in Fig. 2 along with its case, comprises an array of 64 LYSO crystal pixels divided in 4 blocks (each block is 4×4 crystals), with a pixel pitch of approximately 6.3 mm. To ensure sufficient detection efficiency, the LYSO scintillator has a thickness of 30 mm, providing a theoretical efficiency ranging from 55% (for 3-MeV gamma rays) to 45% (for 7-MeV gamma rays). The efficiency estimation was obtained through Lambert–Beer law[47] and NIST XCOM database[48] and considering any kind of photon interaction that can take place in the scintillator.

The LYSO scintillator is coupled in a 1:1 configuration with Near-Ultraviolet High Density (NUV-HD) silicon photomultipliers (SiPMs) from Fondazione Bruno Kessler (FBK (https://www.fbk.eu), Trento, Italy). The use of SiPM devices with small cell pitch is crucial to have a detector response as linear as possible in the energy range of interest (3–7 MeV). In 1:1 configuration, most of the light generated by high-energy gammas in a crystal pixel is read out by a single SiPM and therefore could saturate the sensor response if the number of photons is not smaller than the number of SiPM microcells[49]. For this reason, the cell pitch chosen for the SiPMs is 15 µm. These SiPMs offer a Photon Detection Efficiency (PDE) measured by the manufacturer between 20 and 40% at 420 nm (LYSO peak emission wavelength), depending on the applied overvoltage[50].

The readout electronics is based on four 16-channel GAMMA Application-Specific Integrated Circuits (ASICs)[51], which concurrently read the signals from all SiPMs and whose output is first digitized and then acquired by a Field Programmable Gate Array (FPGA)-based Data Acquisition (DAQ) system. Additionally, the detector is equipped with a real-time compensation circuit that uses a microcontroller to read a temperature sensor on the SiPM substrate and to regulate the bias voltage applied to them, in order to compensate for the variation of the SiPM breakdown voltage as a function of the temperature (∼25 mV/°C) and therefore avoid gain drifts induced by temperature fluctuations.

Prior to the experimental campaign at CNAO, the energy response of the camera prototype was characterized and calibrated using uncollimated ^{137}Cs (662 keV) and ^{22}Na (511 and 1275 keV) sources. The energy calibration was obtained with a linear fit of the positions of the 511 keV, 662 keV and 1275 keV peaks and making a linear extrapolation to calculate higher energies. During the calibration process, the GAMMA ASIC gain and the SiPMs overvoltage were tuned to have a good photon detection efficiency and to have an output energy dynamic range including the 3–7 MeV energy range, where the most relevant PG lines correlated with beam penetration depth are emitted. The spectroscopic performance of all the channels of the detector was also evaluated by calculating for each pixel the energy resolution at the ^{137}Cs peak, defined as the Full Width at Half Maximum (FWHM) of a Gaussian fit of the peak divided by the position of the peak.

The positioning capability of the photodetection module was experimentally verified at the INFN laboratory in Milano, Italy. The process involved scanning the LYSO array along a row of pixels with a collimated ^{137}Cs in steps of 2 mm. The source was collimated using a tungsten-based alloy collimator featuring a 1 mm aperture, positioned 7 cm away from the detector. The detector was aligned and moved using a pair of linear translation stages. With this setup, the position sensitivity was assessed by measuring the number of counts on the different pixels as a function of the beam position, checking that for a certain beam position the corresponding illuminated pixel(s) would increase their count rate.

PGI experimental setup and data acquisition at CNAO

As mentioned before, PGI experiments were performed at the Centro Nazionale di Adroterapia Oncologica (CNAO) in Pavia, Italy. The measurement campaign had two main aims: first, to investigate if the spatial correlation between the Bragg peak position and the PG signal profile along the beam axis is maintained even in the high neutron background of CIRT. Second, to characterize the sensitivity of the PGI system in determining the C-ion range for different number of incident carbon ions and in particular for the delivery of an average irradiation spill to the phantom ($10^7 - 10^8$ carbon ions). It is worth noting that the gamma camera used in the experiment ($5 \times 5 \times 3$ cm^3) is four times smaller than the camera siumulated with FLUKA ($10 \times 10 \times 3$ cm^3) and that in FLUKA simulations the contribution to the background due to the irradiation room was not simulated, but only the background due to the phantom and the collimator was present.

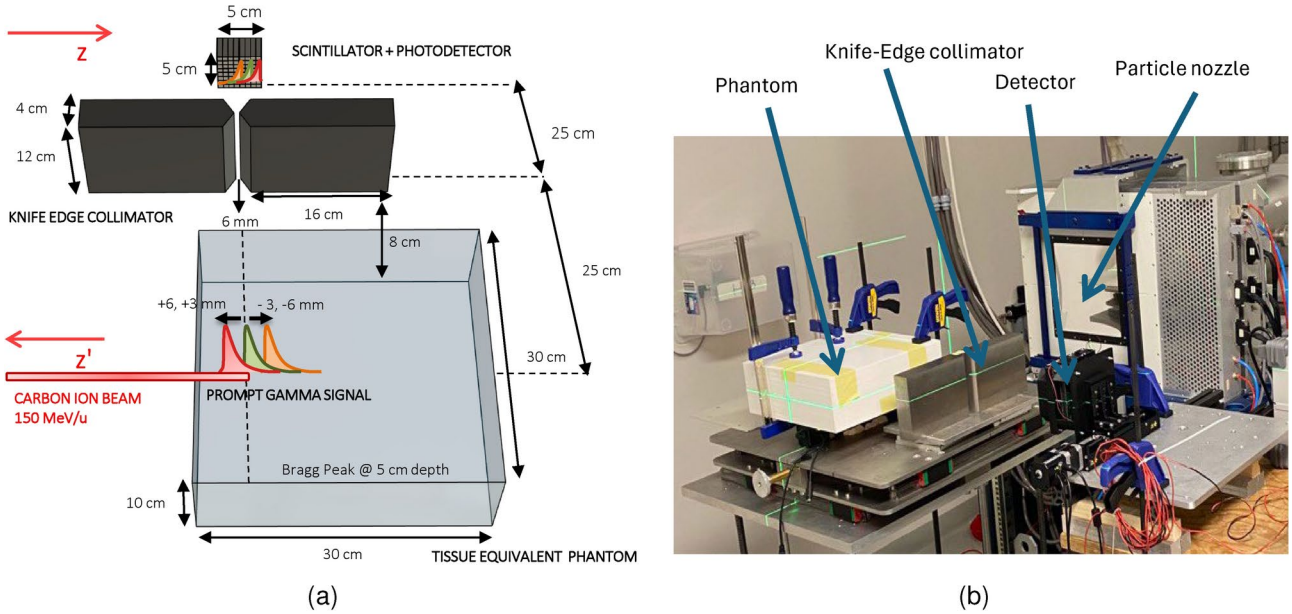

Fig. 3. (**a**) Knife Edge Slit Camera setup configuration at CNAO; the phantom and collimator axes, as well as the collimator axis and detector face, are separated by 25 cm. (**b**) Photo of the measurements setup at CNAO.

As illustrated in Fig. 3, during the experimental campaign at CNAO, the collimator axis and the face of the detector were positioned at distances of 25 cm and 50 cm from the beam axis, respectively. The phantom used in the experiments was a $30 \times 30 \times 10$ cm^3 phantom composed of ten slabs ($30 \times 30 \times 1$ cm^3) of RW3 material, provided by CNAO. This material consists of white polystyrene with a mass percentage of 2% T_iO_2 and possesses physical properties intermediate between water and polymethylmethacrylate (PMMA) phantoms with a density of 1.045 g/cm^3 (https://www.ptwdosimetry.com/en/products/rw3-slab-phantom). The beam was irradiated approximately at the center of a 30×10 cm^2 face of the phantom (at the center of one slab) along the axis of the phantom, resulting in a face to face collimator-phantom distance of 8 cm. This arrangement provided a field-of-view (FOV) of 5 cm on the phantom along the beam axis and the gamma camera was positioned so that the center of this FOV was aligned with the expected range of the impinging carbon ions. Theoretical calculations indicate that the camera system (detector + collimator) in this configuration has a total imaging spatial resolution, evaluated as the Full Width at Half Maximum (FWHM) of the Point Spread Function (PSF), of approximately 23 mm[52]. This resolution derives from a combination of the crystal pixel pitch, knife edge aperture and relative distances contributions. This camera resolution smooths the 1D image of the PG profile, however, since the beam range shifts are estimated measuring the shifts of the total PG distribution, it is still adequate to obtain a precision of a few millimeters[35].

The phantom was positioned on a linear stage moving along the direction of the beam axis. Irradiation was conducted using fixed, mono-energetic carbon-ion pencil beams. The beam energy was set to 150 MeV/u, within the clinical energy range, with the expected Bragg peak depth corresponding to 5 cm. The phantom central position on the moving stage was defined so that the Bragg peak position would be in the beam isocenter and this position would be perpendicularly aligned with the center of the collimator slit.

Using this experimental setup, an extensive set of PGI measurements were acquired over two different runs, performed in different days. During the measurements, Bragg-peak position shifts were induced by altering the phantom position along the beam direction. In part of the measurements, also the detector was moved in parallel to the beam direction using a second linear stage, in order to acquire the PG profile across a wider field-of-view (FOV), similar to the one of the simulations.

In order to have large datasets of events and to be able to study the dependence of the particle range retrieval precision from the number of delivered ions using small subsets of the total dataset, for each phantom/detector configuration the phantom was irradiated with a dose equal to 100 spills of $8 \cdot 10^7$ carbon ions, totaling $8 \cdot 10^9$ ions, similarly to the procedure which was followed in the MC study. The beam current for each spill was 3.2 pA, which is within the clinical current range.

In the first measurement run, which will be denoted as Run 1, the phantom was translated in 3 mm steps along the beam direction using the linear translator, resulting in 5 Bragg peak positions with respect to the center of the collimator, i.e. $-6, -3, 0, +3, +6$ mm. Negative shifts of the linear stage correspond to movements of the phantom away from the beam nozzle (see orientation of Z′ axis in Fig. 3a). In this run, for each phantom position, also the detector prototype was moved in other 2 positions in addition to the one aligned with the collimator slit, in order to acquire the data across a total FOV of ~ 12.6 cm. In detail, for each position of the phantom, the detector was moved along the beam direction back and forth from the central position and for each detector position the PG profiles were acquired so that they would overlap for 3 pixels with the nearby

measurements in order to have enough points in the profiles to link them at the borders, as it will be discussed in the next section.

For each of the three possible detector positions, a background measurement was also acquired. Due to the limited time available to complete all the measurements and the minimal expected changes in the acquired background data for such small deviations in the phantom position, measurements were acquired only for the reference position of the phantom. The measurement was obtained completely closing the collimator, i.e. rotating 180 degrees both the collimator block around their vertical axis, placing in contact the right-angled faces of the two collimator blocks, and irradiating the phantom in the central position with the same dose as for the other measurements.

In the second experimental run, denoted as Run 2, the same setup configuration of the first run was used but measurements were acquired for different phantom positions (− 4, − 2, 0, + 2, + 4) mm and the detector was not moved to extend the FOV.

Data processing

In all measurements (detector characterization and PGI acquisitions), acquired data were first processed to estimate the position of interaction and the energy deposit of each event.

For each event acquired by the pixelated detector, 64 values corresponding to the light signals read by each SiPM are saved. The position of interaction of the event triggering the acquisition was estimated assigning the event to the crystal pixel above the SiPM reading the highest light signal, under the assumption of maximum energy deposition in the crystal pixel where the gamma ray interacts.

Once the events were assigned to a crystal pixel, separate energy spectra were created for each pixel, considering only the events assigned to that crystal and using only the energy value read by the corresponding SiPM. As mentioned before, the calibration of each spectrum was obtained separately through dedicated measurements with uncollimated ^{22}Na and ^{137}Cs sources.

LYSO crystals have a considerable internal background activity due to the decay of the ^{177}Lu naturally present inside the crystals. Therefore, during the data pre-processing procedures performed for both the measurements to verify the positioning performance of the detector and the energy calibration measurements, the spectrum of the LYSO background (measured separately) was routinely subtracted from the spectrum of each pixel before the spectrum analysis. For consistency, this step was maintained also for the PGI measurements, even if the LYSO intrinsic radioactivity features decay energies up to about 1.2 MeV, which are lower than the energies of interest in these measurements.

In PGI measurements, the PG profiles were obtained calculating the total number of counts in the 3–7 MeV energy range for each pixel channel. These counts were then summed along all pixel columns perpendicular to the beam axis to obtain 8 values, yielding the 1D PG profile. The same data processing was applied for measurements with the closed collimator. The final PG profiles used for range estimation were obtained subtracting the background profiles measured with the closed collimator from the total profiles (using for each measurement the background profile obtained for the same position of the detector).

In the measurements of Run 1, in which the PG profiles for different detector positions were measured, two PG profiles were considered during the analysis. First, only the PG profile acquired with the detector aligned with the center of the slit collimator. Second, an extended PG profile calculated as the sum of the three separate profiles measured with the detector in three different positions. For this second profile, the interconnection points of the 3 detector shift datasets were calculated by computing the mean value for each overlapping pair of pixels.

For each run, the PG curve with 0 mm phantom shift was considered the reference profile and fitted with an empirical function. In Run 1, the empirical function used for the PG profile with extended FOV (12.6 cm total) was the sum of two Gaussian functions, whereas in Run 1 with small FOV (5 cm) and Run 2 (5 cm), where the PG profiles have smaller equivalent FOV, it was a single Gaussian function. We then assumed that the PG signal shape remains consistent for all phantom shifts and for all subsets with reduced statistics (see analysis below), considering the phantom's homogeneity and the small magnitude of the Bragg-peak shifts. The same function was therefore used to fit the other PG profiles to estimate their shift, keeping the shape of the function constant and using as the only fit parameter a variable representing the shift of the profile along the beam direction (z_{shift}).

For each run and FOV a preliminary evaluation was conducted to assess the deviations of the estimated shifts (z_{shift} values) at high statistic ($8 \cdot 10^9$ C-ions, Fig. 6d) from the expected shift positions: a linear function was then used to fit the measured shift values as a function of the expected shifts in order to evaluate the mean deviation from the estimated Bragg-peak shift positions.

For each measurement (Run 1–5 cm FOV, Run 1–12.6 cm FOV and Run 2–5 cm FOV), an analysis was conducted to estimate the precision in retrieving the particle range for different numbers of carbon ions. From the original total dataset of PG events measured for each phantom position, PG signal curves were derived by randomly dividing the full dataset in subsets of data equivalent to lower statistics: $5 \cdot 10^7$,$1 \cdot 10^8$,$2 \cdot 10^8$,$4 \cdot 10^8$ and $8 \cdot 10^8$ C-ions per subset.

These low-statistic PG curves were fitted with the same Gaussian function as the high-statistic reference curve ($8 \cdot 10^9$ C-ions) and compared with it, calculating for each curve the error in the estimation of its position along the beam axis with respect to the reference curve.

An histogram of counts, accounting for the frequency of reconstructing the particle range in the correct position or in different ones, was obtained for all groups of subsets with reduced statistics, representing the error distribution of the beam-range estimations made for those groups of subsets.

The precision in determining the particle range for each group of subsets was defined as twice the root mean square error (RMSE) value (2σ), thereby accounting for potential fluctuations and uncertainties in range measurements.

To calculate RMSE value, the sampling extraction process of the subsets was conducted five times, generating new subsets each time. From these iterations, distinct RMSE values were derived, facilitating a comprehensive evaluation of measurement variability. The RMSE was calculated as follows:

$$RMSE = \sqrt{(z_{shift_h} - z_{shift_l})^2} \tag{1}$$

where z_{shift_h} and z_{shift_l} represent the position of the peak of the curve at high statistics and the one at low statistics, respectively.

When evaluating the precision of the RMSE estimate, we accounted for the error associated with its determination. This entailed calculating the ratio between the estimated RMSE for each iteration and the square root of twice the number of subsets minus 1, as specified in the following expression:

$$RMSE_{err} = \frac{\sigma}{\sqrt{2 \cdot (N-1)}} \tag{2}$$

where σ represents the RMSE previously calculated and N is the number of sub-datasets.

Further refining the assessment, the precision has been computed as the mean of twice the RMSE values obtained from the five iterations. Additionally, the error associated with this precision metric was determined by averaging the five errors calculated during the different sampling processes.

Results

Irradiating the detector with uncollimated ^{137}Cs (662 keV) and ^{22}Na (511 and 1275 keV) calibration sources, we obtained energy spectra such as the ones depicted in Fig. 4, which are related to one quadrant of the detector (16 channels) when irradiated by ^{137}Cs source. In the same figure, the energy resolution at 662 keV of all the channels is also reported, which is evaluated as Full Width at Half Maximum (FWHM) of the Gaussian fitting centered in the photo-peak value, resulting on average comprised between 15 and 20%.

From the position sensitivity analysis conduced with ^{137}Cs collimated radioactive source, we obtained the count-rate response curves of the different pixels. Figure 5 shows the number of counts in the 8 pixels along the irradiation path for each position of the radioactive source during the scan after the subtraction of LYSO background contribution: as expected, the plot shows an increase in the counts in each pixel when the irradiation reaches them, with a maximum value when the collimated source is positioned nearby the center of the pixel.

We can conclude that the detector response is consistent with to the detector structure (1:1 coupling between crystals and SiPMs) and has a spatial resolution in the order of 6 mm (equal to the crystal pitch), which does not provide a relevant contribution to the theoretical total resolution of the gamma camera (23 mm).

For the sake of simplicity, graphical representations of the PG profiles will only be provided for the results pertaining to Run 1 with a 12.6 cm field of view (FOV). Discussion of the results obtained from measurements with a 5 cm FOV in Run 1 and Run 2 will be conducted without graphical support, as the figures are similar to the ones that will be presented for the extended FOV dataset.

During the measurement session at CNAO, the knife-edge slit camera captured five one-dimensional prompt gamma profiles corresponding to the five shifts of the phantom. These profiles are depicted in Fig. 6a, along with the profile obtained with the closed collimator. For visualization purposes, the experimental points are connected with lines. The pixels at the detector edges exhibit higher counts, which were not observed in laboratory tests with radioactive sources and were not present in MC simulations. This discrepancy can probably be attributed to external factors, such as background generated by the experimental room during irradiations. Apart from this phenomenon, the total profile with closed collimator appears to have a rather flat trend. This signal is subtracted from the total measured profiles with open collimator in order to get rid of part of uncorrelated signal, mainly due to neutron emissions and other forms of secondary radiation. After subtracting the data related to closed collimator from the total detected profile, the resulting PG profiles are depicted in Fig. 6b.

The PG curve with 0 mm shift is considered the reference curve and it is fitted with a function made by a sum of two Gaussian functions. For the other PG signal profiles, the same function was applied as the reference PG curve, leaving the shift in the direction of the beam as the only fitting parameter; in Fig. 6c the PG signal curves fitted with a function made by a sum of two Gaussian functions are represented for each phantom shift along with the original experimental data. We made the approximation that all the PG signal shapes for different phantom shifts are the same, assuming the phantom is homogeneous and the Bragg-peak shift is small. The goodness of fit was evaluated for all five shift curves, resulting in an R-squared value higher than 85%. This indicates that the chosen model function adequately explains the variance in the dependent variable.

Additionally, the normalized root-mean-square error (NRMSE) was evaluated for all five curve fittings, resulting in a value lower than 39%. This suggests a moderate fit accuracy, indicating that there are some errors in the prediction but the model still captures a relevant portion of the variation in the data. It can be noticed that the shifts in the PGI curves are noticeable and consistent with the phantom shifts.

From the analysis about the mean deviation between the measured shift positions and the predicted ones from a linear extrapolation, an average deviation of 0.24 mm was obtained. This parameter was also evaluated for the Run 1 and Run 2 in the case of 5 cm FOV obtaining a mean deviation of 0.41 mm and 0.35 mm respectively.

Further analysis was carried out to estimate the precision in retrieving the particle range for different numbers of carbon ions. PG signal curves were derived from the original dataset of the reference curve (at $8 \cdot 10^9$ carbon ions) by using subsets of data equivalent to lower statistics: $5 \cdot 10^7$,$1 \cdot 10^8$,$2 \cdot 10^8$,$4 \cdot 10^8$ and $8 \cdot 10^8$ carbon ions.

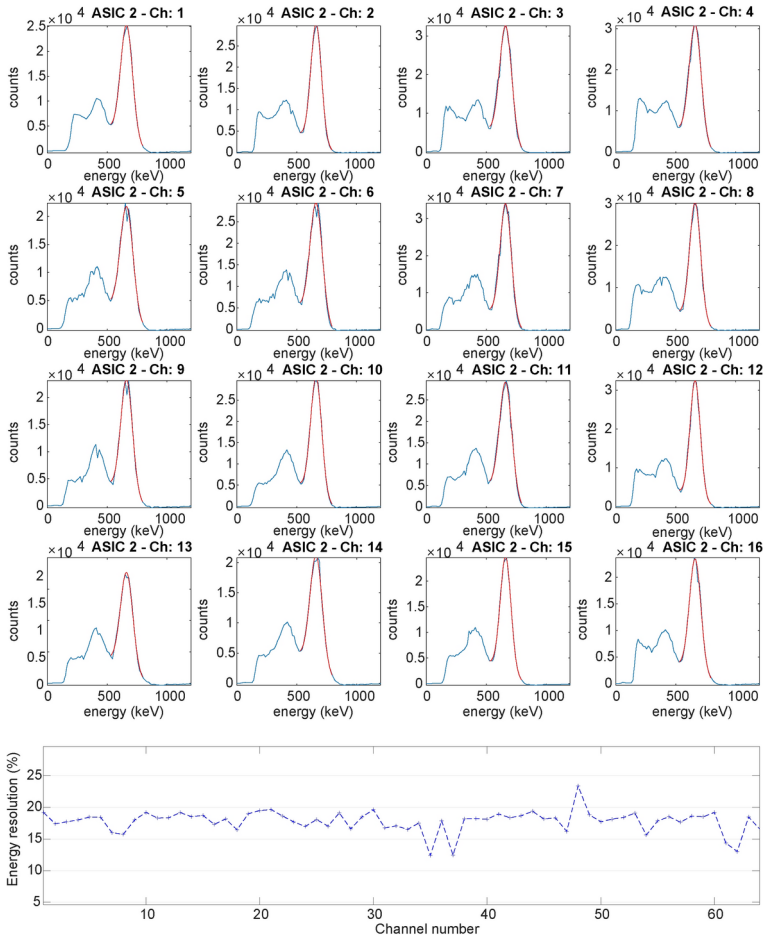

Fig. 4. Top: Energy spectra of one quadrant of the detector (16 channels) when irradiated with an uncollimated ^{137}Cs source. Bottom: Energy resolution at 662 keV of all the detector channels.

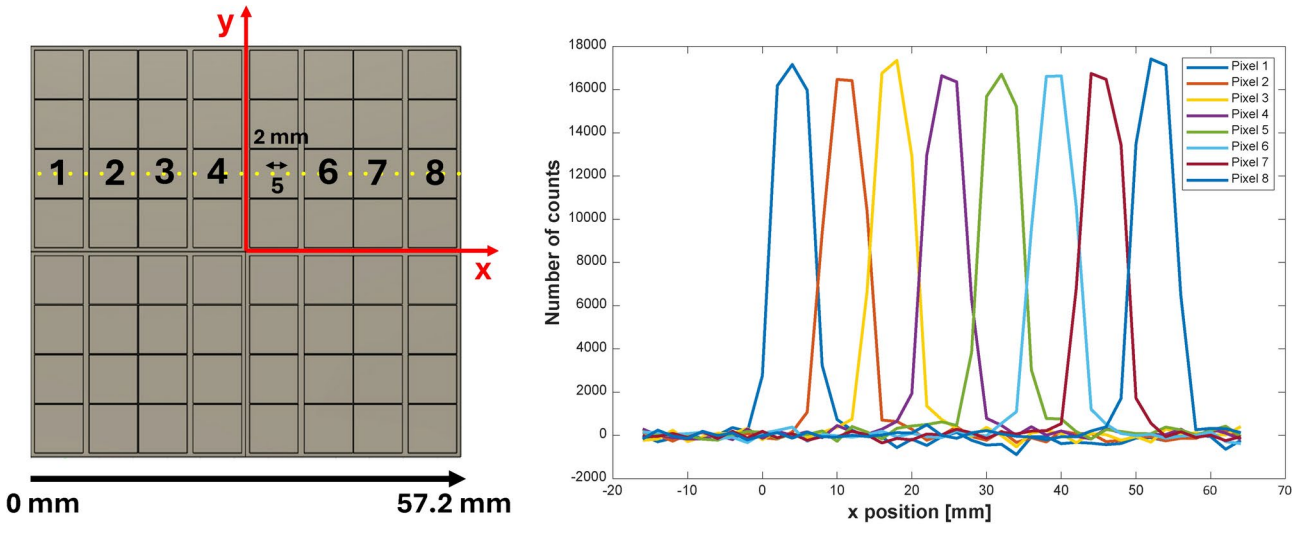

Fig. 5. (**a**) A 1-mm-collimated ^{137}Cs source irradiates the detector which is moved along the × direction in steps of 2 mm. (**b**) Spatial response of the 8 scanned pixels: for each position of the ^{137}Cs collimated source, the number of counts of each pixel is plotted.

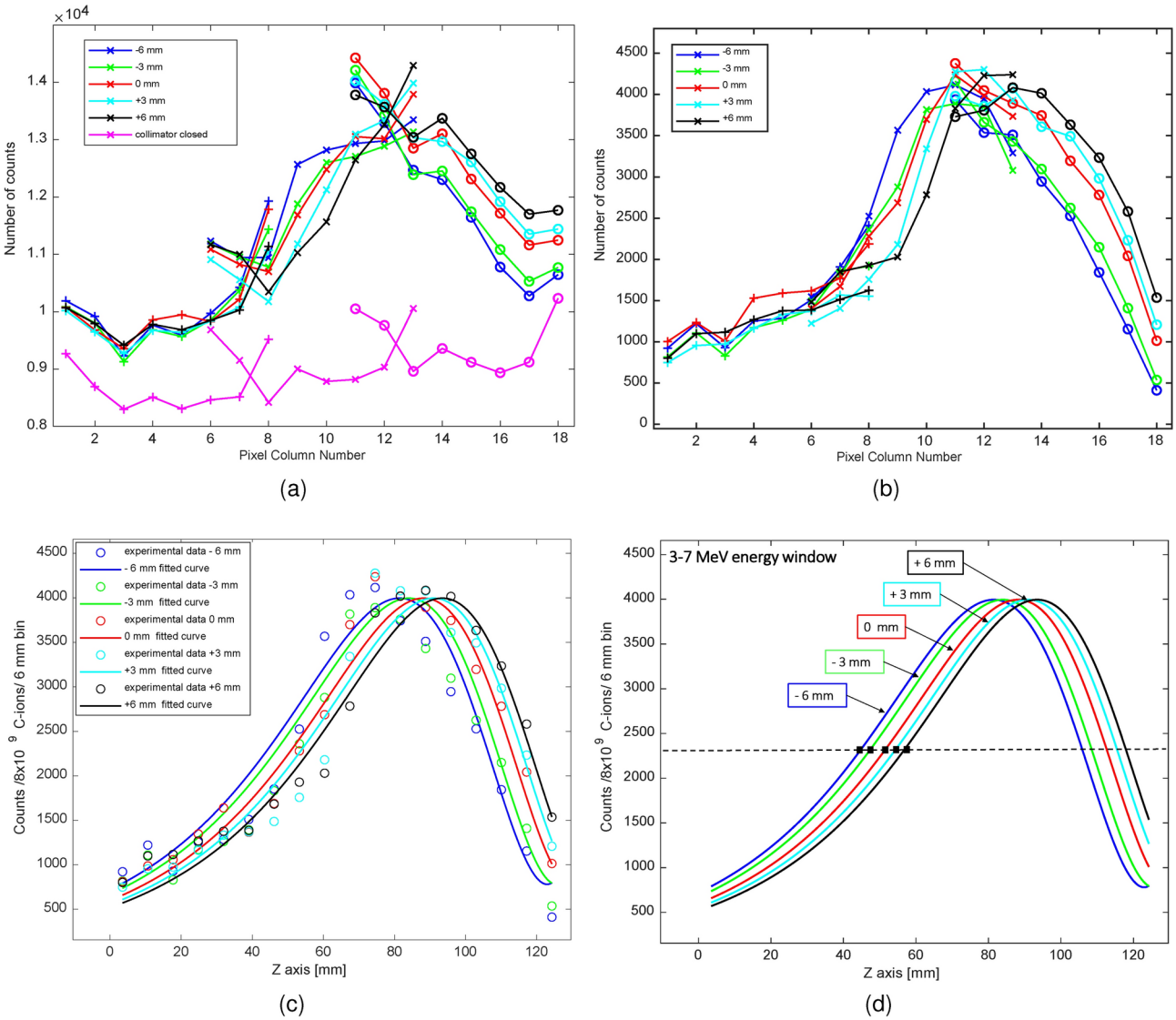

Fig. 6. PG profiles with extended FOV (Run 1–12.6 cm) corresponding to the 5 phantom shifts of − 6, − 3, 0, + 3 and + 6 mm (3–7 MeV energy window): (**a**) detected PG signals (without subtracting the profiles with closed collimator) along with the profiles measured with closed collimator; (**b**) detected PG signal after subtracting the background profiles measured with closed collimator; (**c**) the PG experimental data (circles) along with their Gaussian fits. (**d**) the relative shift positions along the Z axis of the PG signal curves used for the mean deviation shift analysis.

These low-statistic PG curves were fitted with the same Gaussian function as the high-statistic reference curve and compared with it. For each of these curves, the position deviation from the reference curve along the beam axis was estimated (Fig. 7a).

For all the statistics, an histogram of counts is obtained, representing the frequency of reconstructing the Bragg-peak position in the correct position or in different ones. The histograms of the deviations of the estimated Bragg-peak position for the low-statistics PG curves from the position estimated of the reference curve at 0 mm shift with high statistics is depicted in Fig. 7b for the different number of carbon ions considered ($5 \cdot 10^7$,$1 \cdot 10^8$, $2 \cdot 10^8$,$4 \cdot 10^8$ and $8 \cdot 10^8$). Increasing the number of particles considered in each subset leads to a reduction in the dispersion of the range-position deviation, resulting in a more precise reconstruction of the particle range.

In Fig. 8a, the precision in reconstructing the particle range is represented on a double logarithmic scale. This precision is depicted as a function of the number of carbon ions impinging on the phantom, in the case of Run 1–12.6 cm FOV for the different Bragg-peak shifts. A linear interpolation is applied to the data achieving a slope of $\sim -0.48, -0.51, -0.50, -0.53, -0.52$ for the − 6, − 3, 0, + 3, + 6 mm Bragg-peak shifts respectively. From these results, it can be inferred that the precision estimation values obtained for various statistics remain consistent across the different PG shift curves and follow the expected trend proportional to the inverse of the square root of the number of impinging carbon ions (N_{ions}), as for the FLUKA simulations: $2\sigma_{shift} \propto \frac{1}{\sqrt{N_{ions}}}$.

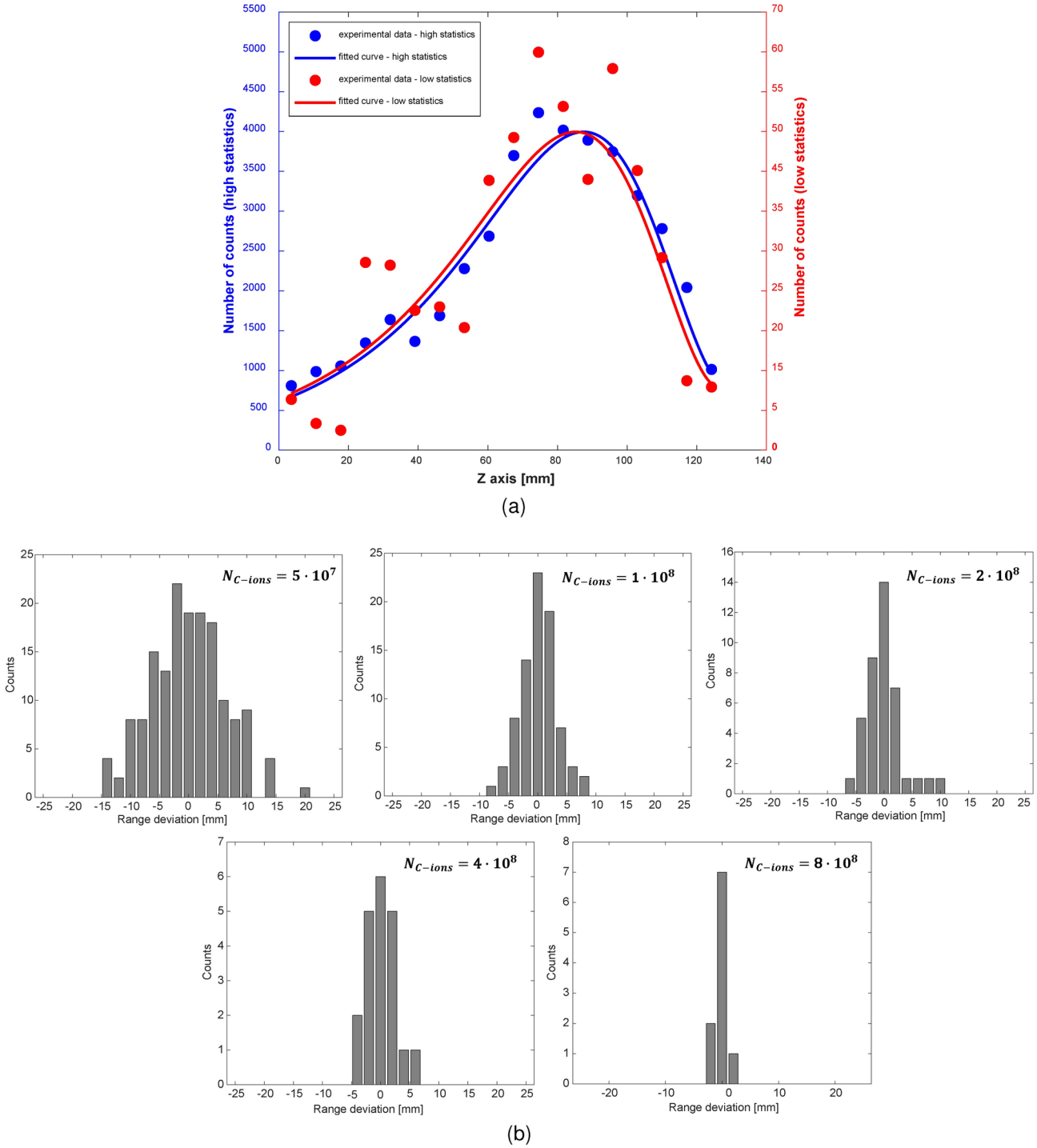

Fig. 7. (**a**) Example of a low statistics curve (red dots and red fitting) at $1 \cdot 10^8$ carbon ions compared with the high statistics curve at 0 mm shift (blue dots and blue fitting) at $8 \cdot 10^9$ carbon ions for the determination of the Bragg-peak shift along the beam axis (Run 1–12.6 cm FOV). (**b**) Histograms of the range deviation of the low statistics PG curves (Run 1–12.6 cm FOV) from the expected range derived from the PG reference curve at high statistics for different number of carbon ions: $5 \cdot 10^7$, $1 \cdot 10^8$, $2 \cdot 10^8$, $4 \cdot 10^8$ and $8 \cdot 10^8$.

In Fig. 8b is shown in a double logarithmic plot the precision in reconstructing the particle range as a function of the number of carbon ions impinging in the phantom along with the error bars. The precision in this graph is obtained considering just the 0-mm-shift position of the phantom in the case of Run 1–5 cm FOV, Run 1–12.6 cm FOV and Run 2–5 cm FOV. It can be inferred that the consistency in precision values between the two experimental runs, notably in the high statistics scenario, indicates a good degree of repeatability in the

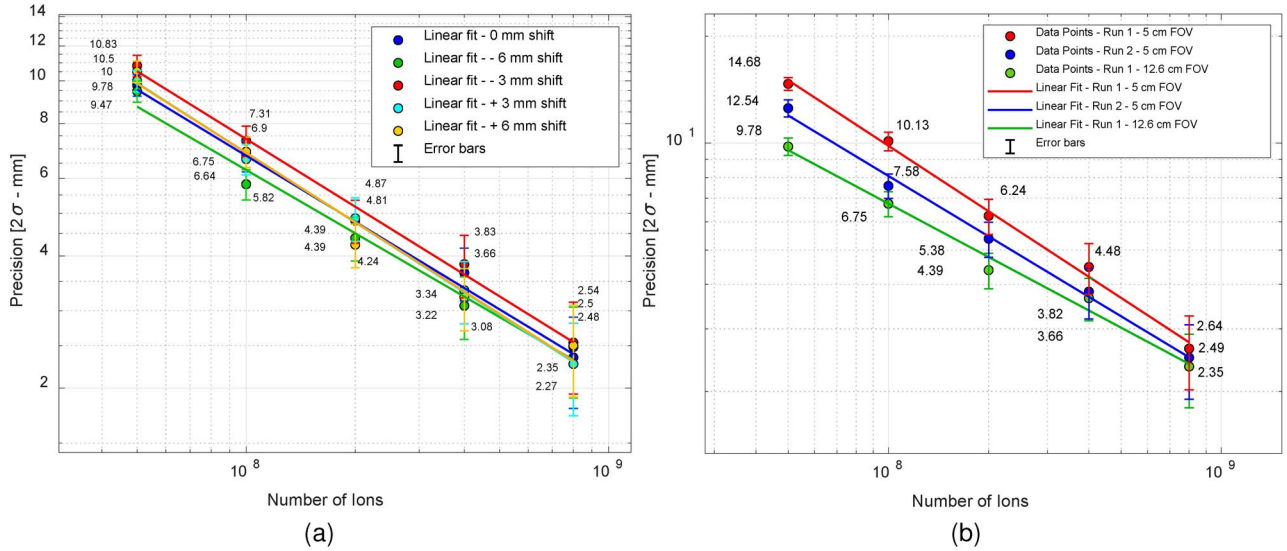

Fig. 8. (**a**) Precision in retrieving the particle range for different number of carbon ions in double logarithmic scale for Run 1–12.6 cm FOV for − 6, − 3, 0, + 3, + 6 mm Bragg-peak shifts. A linear interpolation of the data is applied. (**b**) Same plot as (**a**) for the 0-mm-shift curves for Run 1 (5 cm and 12.6 cm FOV) and Run 2 (5 cm FOV).

measurements. Moreover it is evident that extending the field of view of the slit camera results in an improvement in precision.

Discussion and conclusions

This study focuses on the detectability of Bragg-peak shifts, assuming a prompt gamma (PG) reference profile is available for comparison with the measured profile. In clinical applications, this reference profile will typically be a simulated one and, for example, can be based on Computed Tomography (CT) as used in some studies[42,43]. If the statistic necessary to achieve the desired precision is collected when the total daily fraction is delivered, PGI information can be used to compensate for possible errors in the following fractions, a result which would still be of fundamental importance in clinical practice. If the required statistic is collected when only a small part of the daily fraction is delivered, then this information can even be used to decide whether to complete the fraction or to stop it, e.g. if the peak shift is larger than the safety margin foreseen in the treatment plan.

With the prototype detector presented in this paper, results show that it is possible to measure prompt gamma profiles which can be well-distinguished and are coherent with the phantom shifts also in CIRT. The results indicate that with a FOV of 5 cm, approximately $4 \cdot 10^8$ carbon ions are necessary to estimate with sufficient precision ($2\sigma = 4$ mm) if there were any deviations in the dose deposition position compared to the expected position. In the case of a detector FOV of ~ 13 cm, the number of carbon ions required is instead equal to $3 \cdot 10^8$. These numbers are 8 and 6 times higher than the average spill irradiation ($5 \cdot 10^7$ carbon ions), which ideally would be the portion of the treatment fraction after which the information on a possible Bragg-Peak shift should be available to enable range monitoring and correction within a fraction. Considering that usually in each fraction of a standard treatment cycle the number of delivered carbon ions is in the range of 10^9–10^{10}, the current camera resulted to be capable to assess the particle range with a precision of at least 2.64 mm (at 2σ) following a treatment fraction, thereby potentially compensating for deviations from the treatment plan in subsequent fractions. This would also be the approach that could be most easily integrated with the current patient treatment routine. Therefore, by increasing the area of the detection system, it could even be possible to assess the accuracy of a fraction after a small percentage of the daily dose (< 10%) has been delivered, opening the door to the possibility of making corrections to treatment plans even during a single fraction. A further improvement in the statistics of detected PG rays could be achieved by extending the detector area along the direction perpendicular to the beam axis.

If we scale the experimental results to compensate for the smaller detector area and compare them to MC simulations, we can notice that a higher number of carbon ions is experimentally required to achieve a defined precision than the number estimated with MC simulations. For example, in MC simulations, with a $10 \times 10 \times 3$ cm^3 detector, particle range deviations could be estimated with a precision of approximately 4 mm with a statistics equal to $5 \cdot 10^7$ carbon ions, whereas in experimental measurement, using a $13 \times 5 \times 3$ cm^3 detector, a statistics equal to $3 \cdot 10^8$ is required. However, the higher number of ions required experimentally can be explained by several effects, e.g. the different crystal configuration (slab vs pixels), the non-negligible dead time of the real detector during PGI measurements ($\sim 17\%$), and the higher background in the experimental measurements, since in Monte Carlo simulations the treatment room was not included, which in real measurements increases the number of background events on the detector due to both neutrons and prompt gammas generated by reactions of secondary particles with the material of the room.

In this work, PG profiles were calculated subtracting the closed-collimator background profile, which cannot be practically measured in clinical practice. However, MC simulations and previous measurements with protons show that the background profile due to the phantom and the collimator in the 3–7 MeV range should have a rather flat curve[34,35]. Therefore to subtract it from PGI profiles should not be fundamental to obtain good results during clinical use, as also shown in clinical practice with protons[53]. In this work background subtraction was maintained to reduce an unforeseen high background signal at the detector edges probably due to the background generated by the irradiation room. This issue could reasonably be removed by implementing a proper neutron/gamma-ray shielding on the side and on the back of the detector, which will be introduced in future experiments.

The presented results were obtained with a beam energy equal to 150 MeV/u, at the lower end of the energy range used during clinical carbon-ion treatments. In the case of heavy ions such as carbon ions, at higher energies there is a greater occurrence of neutron emission and temporal overlap between PG and neutrons[54], which translate on a higher background on PG profiles. Therefore, using the same system, a higher number of delivered carbon ions would be needed in order to achieve the same precision, as also found for proton irradiations in previous works[35].

In conclusion, the developed knife-edge camera prototype opens up the possibility of range monitoring and correction within a fraction with a potential reduction of the safety margins usually applied. Indeed, in CNAO's clinical practice, the safety margins for carbon ion radiotherapy are currently set at 3–5 mm for the high-risk clinical target volume (CTV) and an additional 2–5 mm for the low-risk CTV[55]. This is particularly relevant for head and neck cancers, which constitute a substantial portion of CNAO's CIRT clinical activities.

Compared to currently available prototype systems for carbon ion range verification, the proposed PGI systems has (potentially) comparable performance and some advantages. For example, the most advanced in-beam PET scanner achieves millimetric precision in distal fall-off determination for a dose equal to an entire treatment fraction[21], which is comparable with the results that could be achieved with a new PGI prototype with slightly larger area. Moreover, a PGI system could be more easily integrated in treatment rooms since it does not require to have detectors at the opposite side of the patient for coincidence detection, and therefore would be more compatible with the beam delivery systems, especially when movable gantries are present.

For what concerns charged-fragment-detection based range monitoring systems, their main advantage is the counting statistic potentially available and the absence of mechanical collimators, making the system more compact. Experimental studies have shown that most advanced monitoring systems are sensitive to shifts of the fragment origins along the beam axis of at least 1.5 mm for a number of carbon ions equal to $\sim 2 \cdot 10^8$[22]. However, for this systems it might be more difficult to achieve the desired precision in range shift determination for deep seated tumors.

In future work, there is still room for improving the PGI detection system, e.g. introducing an asynchronous reading of pixel data to reduce the data rate and the detector dead time. Furthermore, since a PG photon can interact with multiple pixels following to Compton scattering, leading to multiple interaction events originating from a single gamma ray, improved timing capabilities will also be needed to measure the timestamp of these interactions and correctly process them as belonging to the same event. More advanced strategies to improve the signal to background ratio will also be studied, including the implementation of an optimized, passive shielding for neutrons and gamma rays around the detector or the use of a modified detector capable to perform an active discrimination between the gamma and neutron signals, e.g. by using a scintillator like CLYC[56] which enables the use of the Pulse Shape Discrimination (PSD) technique[57].

Next steps towards the construction of a clinical prototype will also include to investigate the performance of the detection camera in less ideal scenarios, like employing an inhomogeneous phantom and a real treatment planning with the scanning of layers of the phantom and not just considering a single spot irradiation. Furthermore, an accuracy evaluation of the PGI system detected anatomical changes will be carried out with the integration of other imaging devices like Cone Beam Computed Tomography (CBCT) as a ground truth for the determination of the dosimetric variations as already made by other reasearch groups[42,53].

This study is a step forward in in-vivo range verification in CIRT, which could lead to a reduction of safety margins and then of the dose delivered to normal tissues. This marks a significant advancement and increases the potential for enhancing the precision and effectiveness of particle therapy treatments. Overall, our study contributes to advancing the understanding of PGI as a tool for quality assurance in CIRT, offering valuable insights into its potential clinical implementation and highlighting areas for further research and development.

Data availability

The datasets generated during and/or analysed during the current study are available from the corresponding author on reasonable request.

Received: 23 May 2024; Accepted: 11 September 2024
Published online: 28 October 2024

References

1. Particle therapy facilities in clinical operation—Particle therapy co-operative group. https://ptcog.site/index.php/facilities-in-operation-public (2023).
2. Kiseleva, V. *et al.* Particle therapy: Clinical applications and biological effects. *Life* **12**, 2071. https://doi.org/10.3390/life12122071 (2022).
3. Yang, M. *et al.* Comprehensive analysis of proton range uncertainties related to patient stopping-power-ratio estimation using the stoichiometric calibration. *Phys. Med. Biol.* **57**, 4095–4115. https://doi.org/10.1088/0031-9155/57/13/4095 (2012).

4. Paganetti, H. *et al.* Roadmap: Proton therapy physics and biology. *Phys. Med. Biol.* **66**, 05RM01. https://doi.org/10.1088/1361-6560/abcd16 (2021).
5. Fattori, G. & Riboldi, M. Dosimetric effects of residual uncertainties in carbon ion treatment of head chordoma. *Radiat. Oncol.* **113**, 66–71. https://doi.org/10.1016/j.radonc.2014.08.001 (2014).
6. Taasti, V. T., Jeong, J., Jackson, A. & Deasy, J. O. A theoretical investigation of adequate range uncertainty margins in proton treatment planning to preserve tumor control probability. *Acta Oncol.* **58**, 1446–1450. https://doi.org/10.1080/0284186X.2019.1627415 (2019).
7. Knopf, A. C. & Lomax, A. In vivo proton range verification: A review. *Phys. Med. Biol.* **58**, 131–160. https://doi.org/10.1088/0031-9155/58/15/R131 (2013).
8. Pausch, G. *et al.* Detection systems for range monitoring in proton therapy: Needs and challenges. *Nucl. Instrum. Methods Phys. Res. A: Accel. Spectrom. Detect. Assoc. Equip.* **954**, 161227. https://doi.org/10.1016/j.nima.2018.09.062 (2020).
9. Krimmer, J., Dauvergne, D., Létang, J. M. & Testa, É. Prompt-gamma monitoring in hadrontherapy: A review. *Nucl. Instrum. Methods Phys. Res. A: Accel. Spectrom. Detect. Assoc. Equip.* **878**, 58–73. https://doi.org/10.1016/j.nima.2017.07.063 (2018).
10. Parodi, K. & Polf, J. C. In vivo range verification in particle therapy. *Med. Phys.* **45**, e1036–e1050. https://doi.org/10.1088/0031-9155/58/15/R131 (2018).
11. Wrońska, A. & Dauvergne, D. Range verification by means of prompt-Gamma detection in particle therapy 1. In *Radiation detection systems* 139–160 (CRC Press, Boca Raton, 2021). https://doi.org/10.1201/9781003218364.
12. Cheon, B.-W. & Min, C. H. Prompt gamma imaging system in particle therapy: A mini-review. *Front. Phys.* **12**, 1356572. https://doi.org/10.3389/fphy.2024.1356572 (2024).
13. Piersanti, L. *et al.* Measurement of charged particle yields from PMMA irradiated by a 220 Mev/u 12C beam. *Phys. Med. Biol.* **59**, 1857. https://doi.org/10.1088/0031-9155/59/7/1857 (2014).
14. Enghardt, W. *et al.* Charged hadron tumour therapy monitoring by means of PET. *Nucl. Instrum. Methods Phys. Res. A: Accel. Spectrom. Detect. Assoc. Equip.* **525**, 284–288. https://doi.org/10.1016/j.nima.2004.03.128 (2004).
15. Mizuno, H., Tomitani, T., Kanazawa, M., Kitagawa, A. & Pawelke, J. Washout measurement of radioisotope implanted by radioactive beams in the rabbit. *Phys. Med. Biol.* **48**, 2269–81. https://doi.org/10.1088/0031-9155/48/15/302 (2003).
16. Shakirin, G. *et al.* Implementation and workflow for PET monitoring of therapeutic ion irradiation: A comparison of in-beam, in-room, and off-line techniques. *Phys. Med. Biol.* **56**, 1281–1298. https://doi.org/10.1088/0031-9155/56/5/004 (2018).
17. Toramatsu, C. *et al.* Measurement of biological washout rates depending on tumor vascular status in 15O in-beam rat-PET. *Phys. Med. Biol.* **67**, 125006. https://doi.org/10.1088/1361-6560/ac72f3 (2022).
18. Parodi, K., Yamaya, T. & Moskal, P. Experience and new prospects of PET imaging for ion beam therapy monitoring. *Z. Med. Phys.* **33**, 22–34. https://doi.org/10.1016/j.zemedi.2022.11.001 (2023).
19. Ferrero, V. *et al.* Online proton therapy monitoring: Clinical test of a Silicon-photodetector-based in-beam PET. *Sci. Rep.* **8**, 4100. https://doi.org/10.1038/s41598-018-22325-6 (2018).
20. Fiorina, E. *et al.* Detection of interfractional morphological changes in proton therapy: A simulation and in vivo study with the INSIDE in-beam PET. *Front. Phys.* **8**, 578388. https://doi.org/10.3389/fphy.2020.578388 (2021).
21. Pennazio, F. *et al.* Carbon ions beam therapy monitoring with the INSIDE in-beam PET. *Phys. Med. Biol.* **63**, 145018. https://doi.org/10.1088/1361-6560/aacab8 (2018).
22. Kelleter, L. *et al.* An in-vivo treatment monitoring system for ion-beam radiotherapy based on 28 Timepix3 detectors. *Sci. Rep.* **14**, 15452. https://doi.org/10.1038/s41598-024-66266-9 (2024).
23. Fischetti, M. *et al.* Inter-fractional monitoring of 12 C ions treatments: Results from a clinical trial at the CNAO facility. *Sci. Rep.* **10**, 20735. https://doi.org/10.1038/s41598-020-77843-z (2020).
24. Stichelbaut, F. & Jongen, Y. Verification of the proton beams position in the patient by the detection of prompt gamma-rays emission. In *39th Meeting of the Particle Therapy Co-Operative Group, San Francisco, CA*, vol. 16 (2003).
25. Verburg, J. M. & Seco, J. Proton range verification through prompt gamma-ray spectroscopy. *Phys. Med. Biol.* **59**, 7089. https://doi.org/10.1088/0031-9155/59/23/7089 (2014).
26. Hueso-González, F. *et al.* Test of Compton camera components for prompt gamma imaging at the ELBE bremsstrahlung beam. *J. Instrum.* **9**, P05002. https://doi.org/10.1088/1748-0221/9/05/P05002 (2014).
27. Golnik, C. *et al.* Range assessment in particle therapy based on prompt γ-ray timing measurements. *Phys. Med. Biol.* **59**, 5399. https://doi.org/10.1088/0031-9155/59/18/5399 (2014).
28. Min, C., Kim, C., Youn, M. & Kim, J. Prompt gamma measurements for locating the dose falloff region in the proton therapy. *Appl. Phys. Lett.* **89**, 183517. https://doi.org/10.1063/1.2378561 (2006).
29. Xie, Y. *et al.* Prompt gamma imaging for in vivo range verification of pencil beam scanning proton therapy. *Int. J. Radiat. Oncol. Biol. Phys.* **99**, 210–218. https://doi.org/10.1016/j.ijrobp.2017.04.027 (2017).
30. Richard, M.-H. *et al.* Design guidelines for a double scattering compton camera for prompt-gamma imaging during ion beam therapy: A Monte Carlo simulation study. *IEEE Trans. Nucl. Sci.* **58**, 87–94. https://doi.org/10.1109/TNS.2010.2076303 (2010).
31. Aldawood, S. *et al.* Development of a Compton camera for prompt-gamma medical imaging. *Radiat. Phys. Chem.* **140**, 190–197. https://doi.org/10.1016/j.radphyschem.2017.01.024 (2017).
32. Muñoz, E. *et al.* Performance evaluation of MACACO: A multilayer Compton camera. *Phys. Med. Biol.* **62**, 7321. https://doi.org/10.1088/1361-6560/aa8070 (2017).
33. Draeger, E. *et al.* 3D prompt gamma imaging for proton beam range verification. *Phys. Med. Biol.* **63**, 035019. https://doi.org/10.1088/1361-6560/aaa203 (2018).
34. Smeets, J. *et al.* Prompt gamma imaging with a slit camera for real-time range control in proton therapy. *Phys. Med. Biol.* **57**, 3371. https://doi.org/10.1088/0031-9155/57/11/3371 (2012).
35. Perali, I. *et al.* Prompt gamma imaging of proton pencil beams at clinical dose rate. *Phys. Med. Biol.* **59**, 5849. https://doi.org/10.1088/0031-9155/59/19/5849 (2014).
36. Priegnitz, M. *et al.* Measurement of prompt gamma profiles in inhomogeneous targets with a knife-edge slit camera during proton irradiation. *Phys. Med. Biol.* **60**, 4849. https://doi.org/10.1088/0031-9155/60/12/4849 (2015).
37. Pinto, M. *et al.* Design optimisation of a TOF-based collimated camera prototype for online hadrontherapy monitoring. *Phys. Med. Biol.* **59**, 7653. https://doi.org/10.1088/0031-9155/59/24/7653 (2014).
38. Kim, J.-W. Pinhole camera measurements of prompt gamma-rays for detection of beam range variation in proton therapy. *J. Korean Phys. Soc.* **55**, 1673–1676. https://doi.org/10.3938/jkps.55.1673 (2009).
39. Sun, S., Liu, Y. & Ouyang, X. Near-field high-resolution coded aperture gamma-ray imaging with separable masks. *Nucl. Instrum. Methods Phys. Res. A: Accel. Spectrom. Detect. Assoc. Equip.* **951**, 163001. https://doi.org/10.1016/j.nima.2019.163001 (2020).
40. Hetzel, R. *et al.* Near-field coded-mask technique and its potential for proton therapy monitoring. *Phys. Med. Biol.* **68**, 245028. https://doi.org/10.1088/1361-6560/ad05b2 (2023).
41. Ready, J. *Development of a multi-knife-edge slit collimator for prompt gamma ray imaging during proton beam cancer therapy*. Ph.D. thesis (UC Berkeley, 2016).
42. Richter, C. *et al.* First clinical application of a prompt gamma based in vivo proton range verification system. *Radiat. Oncol.* **118**, 232–237. https://doi.org/10.1016/j.radonc.2016.01.004 (2016).
43. Berthold, J. *et al.* First-in-human validation of CT-based proton range prediction using prompt gamma imaging in prostate cancer treatments. *Int. J. Radiat. Oncol. Biol. Phys.* **111**, 1033–1043. https://doi.org/10.1016/j.ijrobp.2021.06.036 (2021).

44. Battistoni, G. *et al.* Overview of the FLUKA code. *Ann. Nucl. Energy* **82**, 10–18. https://doi.org/10.1016/j.anucene.2014.11.007 (2015).
45. Missaglia, A. *et al.* Prompt-gamma fall-off estimation with C-ion irradiation at clinical energies, using a knife-edge slit camera: A Monte Carlo study. *Phys. Med.* **107**, 102554. https://doi.org/10.1016/j.ejmp.2023.102554 (2023).
46. Rossi, S. The status of CNAO. *Eur. Phys. J. Plus* **126**, 78. https://doi.org/10.1140/epjp/i2011-11078-8 (2011).
47. Knoll, G. F. *Radiation Detection and Measurement* (Wiley, New Jersey, 2010).
48. Berger, M. XCOM: Photon cross sections database. *figshare*[SPACE]https://physics.nist.gov/PhysRefData/Xcom/html/xcom1.html (2010).
49. van Dam, H. T. *et al.* A comprehensive model of the response of silicon photomultipliers. *IEEE Trans. Nucl. Sci.* **57**, 2254–2266. https://doi.org/10.1109/TNS.2010.2053048 (2010).
50. Gola, A. *et al.* NUV-sensitive silicon photomultiplier technologies developed at Fondazione Bruno Kessler. *Sensors* **19**, 308. https://doi.org/10.3390/s19020308 (2019).
51. Buonanno, L., Di Vita, D., Carminati, M. & Fiorini, C. Gamma: A 16-channel spectroscopic asic for sipms readout with 84-db dynamic range. *IEEE Trans. Nucl. Sci.* **68**, 2559–2572. https://doi.org/10.1109/TNS.2021.3107333 (2021).
52. Bom, V., Joulaeizadeh, L. & Beekman, F. Real-time prompt gamma monitoring in spot-scanning proton therapy using imaging through a knife-edge-shaped slit. *Phys. Med. Biol.* **57**, 297. https://doi.org/10.1088/0031-9155/57/2/297 (2011).
53. Berthold, J. *et al.* Detectability of anatomical changes with prompt-gamma imaging: First systematic evaluation of clinical application during prostate-cancer proton therapy. *Int. J. Radiat. Oncol. Biol. Phys.* **117**, 718–729. https://doi.org/10.1088/1361-6560/aacab8 (2023).
54. Zarifi, M. *et al.* Characterization of prompt gamma ray emission for in vivo range verification in particle therapy: A simulation study. *Phys. Med.* **62**, 20–32. https://doi.org/10.1016/j.ejmp.2019.04.023 (2019).
55. Orlandi, E. *et al.* The role of carbon ion therapy in the changing oncology landscapeâ€a narrative review of the literature and the decade of carbon ion experience at the italian national center for oncological hadrontherapy. *Cancers* **15**, 5068. https://doi.org/10.3390/cancers15205068 (2023).
56. Glodo, J., Hawrami, R. & Shah, K. Development of Cs2LiYCl6 scintillator. *J. Cryst. Growth* **379**, 73–78. https://doi.org/10.1016/j.jcrysgro.2013.03.023 (2013).
57. Roush, M. L., Wilson, M. & Hornyak, W. F. Pulse shape discrimination. *Nucl. Instrum. Methods* **31**, 112–124. https://doi.org/10.1016/0029-554X(64)90333-7 (1964).

Author contributions

A.B.I. and G.B. developed the PGI detection module, conceived and conducted the experiments as well as analysed the results. A.C. and C.R. provided their support for the development of the detector module and during the experimental PGI measurements. M.C. provided his support on the experiment conceptualization and and on the analysis. M.D, M.P. and S.S. organized the beam time for the experimental PGI measurements and provided their support during the irradiations. F.C. provided his support for the detector characterization. C.F. conceived the experiment and gave his support during the experimental PGI measurements and the analysis.

Competing interests

The authors declare no competing interests.

Additional information

Correspondence and requests for materials should be addressed to A.B.I. or C.F.

Reprints and permissions information is available at www.nature.com/reprints.

Publisher's note Springer Nature remains neutral with regard to jurisdictional claims in published maps and institutional affiliations.